# Concept for a novel airborne LiDAR system combining high-resolution snow height mapping with co-registered spatial information on the water content of the snowpack

Lars Rathmann[a,c,*], Joschka Geissler[b], and Alexander Reiterer[a,c]

[a]Albert-Ludwigs-University Freiburg, Department of Sustainable Systems Engineering - INATECH, Emmy-Noether-Straße 2, Freiburg, Germany
[b]Albert-Ludwigs-University Freiburg, Chair of Hydrology, Friedrichstraße 39, Freiburg, Germany
[c]Fraunhofer Institute for Physical Measurement Techniques IPM, Georges-Köhler-Allee 301, Freiburg, Germany

## ABSTRACT

The impact of climate change on snow cover evolution is evident. Increasing amounts of winter precipitation as well as rising temperatures are causing the winter snow cover to change more and more rapidly within one season. To quantify the direct effects on hydrological cycles, spatially and temporally high-resolution information on snow height and the amount of water stored as snow (Snow Water Equivalent, SWE) is required on watershed scales. This paper presents the concept for a novel airborne light detection and ranging (LiDAR) system combining high-resolution snow height mapping with co-registered spatial information on the water content of the snowpack. Based on the optical characteristics of snow, we outline a detailed plan for dual-wavelength LiDAR sensor working at wavelengths of 1030 nm and 515 nm. By comparing the intensities received in the two channels, snow cover parameters like the effective grain size can be inferred. By means of recent snow hydrological models, from these data and the topographic snow depth maps then high resolution SWE maps can be deduced. We supplement our outline with conceptual LiDAR snow depth and reflectance measurements using a commercially available system, pointing out the impact of view angle dependence of received intensity and general applicability for future airborne LiDAR surveys.

**Keywords:** LiDAR, snow depth, airborne, UAV, dual-wavelength, snow-water-equivalent, grain size, snow optics

## 1. INTRODUCTION

The presence of a snow cover significantly affects the global energy budget due to its high surface albedo and serves as a vital water resource in the hydrological cycle for many regions. Accordingly, snow does not only react very sensitively to climate change, but also acts as a central climate feedback component. Therefore, an explicit understanding of snow accumulation and ablation processes under different environmental conditions is of substantial interest. In particular, the presence of vegetation cover such as trees strongly influences aforementioned snow accumulation and ablation processes compared to open areas.[1] To improve the understanding and modelling of these kind of processes under forest vegetation conditions, an extensive data set with high spatial and temporal resolution that captures essential snow parameters is urgently needed. The most straight-forward parameter describing a snow cover for sure is snow depth. Snow depth is commonly defined as the total depth of snow over the ground at a given location and time of observation. This definition includes all older and newer snow layers in the snowpack.[2] In literature there is a large amount of data available ranging from repeated manual field campaign measurements of snowpack depths using snow probes to automated ultra-sonic measurements.[1,3] However, due to its nature, these kind of measurements provide rather sparse spatial and temporal resolution, are time consuming and destructive to the snowpack. Due to the discrete and infrequent data sampling, individual snowfall events and ablation periods between subsequent field campaigns get ignored leading to

*Address all correspondence to Lars Rathmann, E-mail: lars.rathmann@ipm.fraunhofer.de

in: Stella, Ettore; Society of Photo-Optical Instrumentation Engineers – SPIE: Multimodal Sensing and Artificial Intelligence: Technologies and Applications II. Proc. SPIE 11785, Paper 1178513 (2021); doi: 10.1117/12.2591815

substantial estimation biases of accumulation and depletion rates. One way to overcome these issues is to shift snow depth mapping away from the ground to airborne remote sensing platforms like unmanned aerial vehicles (UAV). Recent advances in this technology sector have led to the emergence of a large variety of easy-to-handle and affordable UAVs on the market, such as multicopters of vertical take-off and landing (VTOL) fixed wing gliders. These combine decent payload weight limits with long flight times.

In the framework of remote sensing technology, light detection and ranging (LiDAR) for sure plays a key role and substantial progress in developing this technique has been made in the recent years. The fundamental principle of this technique relies on measuring the round-trip time interval of a laser pulse from the LiDAR scanner to a target and being back-reflected to the receiver. From this measurement, the distance between the target and the receiver can be calculated via the speed of light. In principle, this technique can be employed statically on the ground (terrestrial laser scanning, TLS), on a mobile platform on the ground (mobile laser scanning, MLS) or on a mobile platform in the air, which we refer to as airborne laser scanning (ALS, Fig. 1a). By scanning the laser source over an area of interest and co-registering the position and attitude of the LiDAR scanner for each data point, a geo-referenced point cloud of the surveyed area can be calculated. The process of geo-referencing can be viewed as a transformation of data points $(x_{\mathrm{S}}, y_{\mathrm{S}}, z_{\mathrm{S}})$ measured in the LiDAR scanner's own coordinate system to a fixed reference coordinate system $(x_{\mathrm{R}}, y_{\mathrm{R}}, z_{\mathrm{R}})$, e.g. an earth-centered coordinate system. As illustrated in Fig. 1b, from this point cloud then a digital elevation model (DEM), i.e. a digital height model of the survey area at a certain moment during a season, can be derived. Finally, by subtracting two DEMs measured before and after a snowfall event a topographic map of snow heights $\Delta h$ can be deduced. Performing these kind of surveys frequently throughout a whole winter season, high temporal and spatial resolution data on snow depth evolution during a season can be acquired at much lower expense than a manual survey would need.

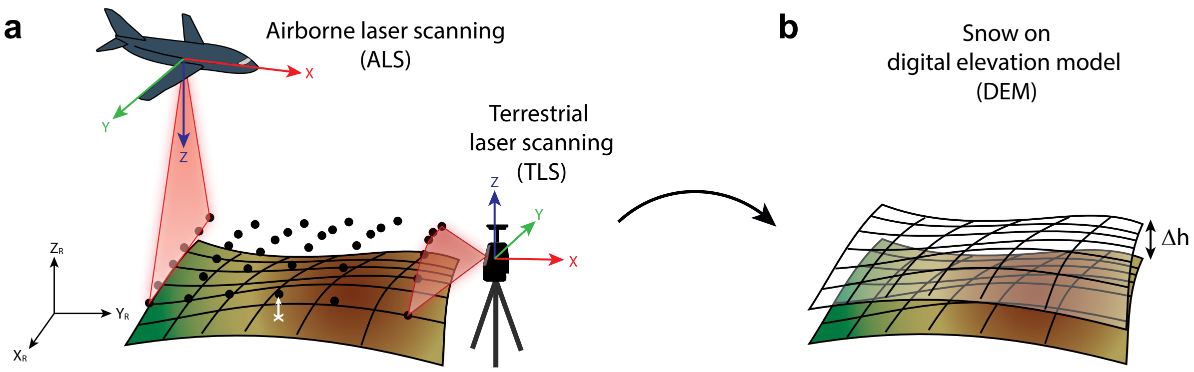


Figure 1: Computation of snow depth maps from LiDAR surveys. **a**, point cloud registration of a snowpack using airborne laser scanning or terrestrial laser scanning. The shaded surface represents the digital elevation model (DEM) of the ground without snow. LiDAR data points have to be geo-referenced, i.e. transformed from local scanner coordinates $(x_{\mathrm{S}}, y_{\mathrm{S}}, z_{\mathrm{S}})$ to fixed reference coordinates $(x_{\mathrm{R}}, y_{\mathrm{R}}, z_{\mathrm{R}})$. **b**, interpolation of a snow on DEM from the point cloud data. The snow depth at a certain position is given by the grid-to-grid distance $\Delta h$.

Asides from snow depth itself, a second crucial snowpack characterization parameter is the amount of water stored in a snowpack, commonly expressed as snow water equivalent (SWE). Nonetheless, SWE is not measurable as straight-forward as snow depth and to our best knowledge, so far there is no LiDAR scanner capable of of capturing information of both, snow depth and SWE in a single measurement.

Here, we propose a concept for a novel airborne LiDAR sensor combining both, high-resolution snow depth mapping with co-registered information of the SWE of the snowpack. The system will be designed as a dual-wavelength laser scanner with one visible channel operating at 515 nm and one near-infrared channel operating at 1030 nm. Whereas the back-reflected intensity in the near-infrared channel is expected to decrease as the effective grain size of the snowpack grows, the intensity in the visible channel should remain mainly unaffected. In a second step, the extracted effective grain size and snow depth together with other environmental data like temperature can then be fed into state-of-the-art snow models to determine the local SWE at each data point. This approach provides a unique combination of cost-effective, non-destructive and multi-temporal mapping of a snow cover on watershed scales. Moreover, using a LiDAR sensor for snow mapping in forested areas has the advantage that there is a finite probability that a laser pulse penetrates the canopy and gets reflected back from the ground below, allowing for precise sub-canopy snow depth mapping. The small form factor and low weight of our proposed solution further supports flexible integration on various UAV platforms. The proposed setup is accompanied by conceptual snow depth and intensity measurements using an already existing commercially available LiDAR scanner, pointing out some of the important peculiarities regarding LiDAR scanning of snow.

## 2. RELATED WORK

In Sec. 2.1 and 2.2 we will give an overview of already existing remote sensing techniques of snow depth and SWE, describing their characteristics and pointing out their advantages and disadvantages.

### 2.1 Remote Sensing of Snow Depth

As already mentioned before, measuring the depth of a snowpack at a certain location is in principle an easy task that can be accomplished using minimalist equipment such as a rod with a scale. However, in most cases this spatial and temporal infrequent kind of data acquisition is insufficient for hydrological models; that is, sparse data like these can lead to erroneous conclusions to be drawn from hydrological models that rely on these data as input. Most of these issues can be addressed by using modern remote sensing techniques based on air- or spaceborne platforms such as planes, drones and satellites.

Contemporary snow depth retrievals from satellite platforms (such as the Sentinel-1) on a watershed scale are mainly based on Synthetic Aperture Radar (SAR) measurements. By illuminating the land surface with C-band microwave radiation (4 to 8 GHz) and analyzing the ratio of backscattered signal in co- and cross-polarization, snow depth maps with a spatial resolution of about $\sim 1\,\mathrm{km}^2$ can be retrieved.[4] Although these systems might deliver valuable data on larger scales, their limited resolution makes them useless for understanding snow processes and variability on smaller scales as in the framework of this publication.[5]

Most certainly, for remote snow depth sensing airborne light detection and ranging (LiDAR) measurements currently provide the most accurate snow depth data.[6] A comprehensive review of snow depth measurements using LiDAR was published by Deems et al.[6] As already outlined before, the fundamental principle of snow height mapping using LiDAR is the range-to-target measurement between a laser scanner and the snow surface. Combining these data with co-registered global navigation satellite system (GNSS) position data of the platform and information of the sensor's attitude, e.g. using an inertial measurement unit (IMU), an elevation model of the surveyed area can be created. Calculating the difference between the snow-free and snow-covered elevation model then gives a spatially resolved map of snow depths.[7] One major advantage of LiDAR measurements over conventional remote sensing techniques is its capability of forest canopy penetration due to high-density point clouds and wide scan angle ranges. These increase the probability of canopy penetration significantly, allowing for sub-canopy mapping of snow characteristics.[6,8]

TLS offers a cost-effective and easy-to-use, but yet accurate way of snow height mapping.[9,10] However, since the data is acquired from a static position, this technique gets limited by obstacles in the line of sight or large incident angles[10] and thus is not optimal for surveying a large area in a feasible manner. For this purpose ALS has proven to be the method of choice. One of the most prestigious projects in the field of airborne LiDAR snow mapping certainly is the Airborne Snow Observatory (ASO) as described by Painter et al.[7] They used a Riegl Q1560 airborne laser scanner, operating with dual 1064 nm wavelength lasers, mounted on an aircraft to map snow height distributions in the western US area. Reported snow depth accuracies on a $15 \times 15\,\mathrm{m}^2$ scale are $< 8$ cm. In addition to its laser scanner, the system was equipped with a CASI 1500 imaging spectrometer for spectral and spectrally-integrated albedo retrievals. Combining the data of these two sensors, additional information on the water content of the snow pack was collected (cf. section 2.2).

Broxton and van Leeuwen quite recently reported an approach combining airborne LiDAR data from a similar platform as Painter et al. with structure from motion (SfM) data measured from a UAV over the same plot.[11]

They could demonstrate that airborne LiDAR outperforms SfM in densely forested regions, whereas in sparsely forested areas both methods give comparable results. Since this is no real surprise, the more important finding is rather that they found a relationship between a small scale SfM map and a previous LiDAR data set over a larger area. From this relationship they infer that multi-temporal SfM maps over selected areas might provide snowpack information of the whole basin at much lower cost than multi-temporal large scale LiDAR surveys.

In a very similar study, Harder et al.[8] compared the capability of UAV-based LiDAR sub-canopy mapping with SfM data of the same plot. LiDAR data collection was performed with a 360° line-scanning Riegl miniVUX-1UAV sensor working at a wavelength in the near infrared regime and geo-referenced using an APX-20 inertial navigation system (INS). As a platform they used a DJI M600 Pro UAV hexacopter. SfM data, on the other hand, were recorded with an eBee X or eBee Plus fixed-wing UAV and RGB cameras from senseFly. Harder et al. found that UAV LiDAR outperforms SfM techniques with root-mean-square errors of $< 0.1\,\mathrm{m}$ and $< 0.17\,\mathrm{m}$ in open and vegetated areas, respectively, compared to $< 0.30\,\mathrm{m}$ and $< 0.33\,\mathrm{m}$. However, they concluded that this gain in accuracy goes along with substantially more expensive equipment and project costs and depending on the project goal, SfM might already yield satisfying results.

Addressing the point of affordability, Jacobs et al. report snow height mapping of a shallow snowpack using a cost-effective LiDAR sensor (Velodyne VLP-16) mounted to an Eagle X8 UAV multicopter.[12] The LiDAR sensor used in this work operates at a wavelength of 903 nm. By means of positional data co-registered by an APX-15 INS unit then the geo-referenced point cloud was calculated, yielding ground point densities of 90 and $364\,\mathrm{points/m^2}$ in the forest and open terrain, respectively. As a result, at a scale of 1 m LiDAR snow depth precision ranged from $< 1\,\mathrm{cm}$ in the open field to $< 4\,\mathrm{cm}$ in vegetated or forest areas, demonstrating the general applicability of such a low-cost system for this purpose.

### 2.2 Remote Sensing of Snow Water Content

Unlike mapping snow depth, mapping the amount of water stored in a snowpack is not as straight forward and needs much more sophisticated methods.[13] As mentioned before, this measured variable is quantified as snow water equivalent (SWE), that is, the depth of water a snowpack would yield when melting completely. For a snowpack of uniform volumetric mass density $\rho_\mathrm{s}$ and depth $h_\mathrm{s}$, the SWE is simply the product of the two quantities. Unless otherwise specified, $\rho_\mathrm{s}$ will be simply referred to as snow density. In reality though, snow undergoes metamorphism processes such as warming and refreezing cycles, compaction or melting runoff, resulting in a depth dependent snow density $\rho_\mathrm{s}(z)$. Accordingly, in general SWE has to be expressed as an integral of the form:

$$\mathrm{SWE} = \frac{1}{\rho_\mathrm{w}} \int_0^{h_s} \rho_\mathrm{s}(z)\,\mathrm{d}z. \tag{1}$$

Note that SWE is normalized to the density of water $\rho_\mathrm{w}$ to give it the dimension of a depth.

In order to determine the SWE of a snowpack, according to eq. (1) the snow depth and corresponding depth depending snow density have to be known. Due to the difficulty of this task, the many publications restrict themselves to determining an effective snow density $\rho_\mathrm{s}$ instead of $\rho_\mathrm{s}(z)$, giving an effective SWE.[14–16]

Early remote sensing techniques for SWE were based on passive sensing of the snow's microwave brightness temperature, e.g. from a satellite or plane. The microwave brightness temperature is related to the snow density and therefore information on the SWE can be extracted. Nonetheless, this technique deals with great uncertainties and is only applicable for rather shallow snowpacks in low-slope terrain.[7,17–19]

Another passive SWE remote sensing approach is to measure the attenuation of natural terrestrial gamma emission from radioisotopes in the ground by a snowpack. Gamma radiation is attenuated by water of any phase and thus, by measuring this radiation once from bare soil and once during the snow season, an integrated SWE can be inferred from the data.[20] Similar to aforementioned technique, this approach is also challenged by complex terrain and canopy cover and does not provide high spatial resolution. In addition, changes of the measured radiation are not necessarily solely linked to the snowpack, but also changes in the soil itself or water content of vegetation.[7]

Contrarily to passive remote sensing techniques, active sensing allows for much more control over the data acquisition. Hence, several active SWE sensing techniques were developed. One idea focuses on interferometric

SAR as discussed by Guneriussen et al.[21] They showed that radar waves acquire a certain phase difference when penetrating a snowpack and being reflected back from the snow-soil interface. This phase difference is very sensitive to changes in SWE and scales linearly with it. Other groups like Rott et al.[22] demonstrated its applicability on airborne platforms and improved this method to account for lost phase cycles or phase wrapping in order to allow for continuous SWE sensing over an entire winter season.[23]

Webb et al.[24] combined similar ground-penetrating radar data measured from a mobile snow sled across their survey area with LiDAR snow depth data delivered by a Riegl VZ-400 terrestrial laser scanner (TLS) to quantify the bulk LWC distribution of a snowpack. Employing this method, local LWC variations from zero to 19 % were detected, as well as rapid LWC changes of up to 5 % on a subdaily timescale. Also quite recently, Pomerleau et al.[25] demonstrated a low-cost, compact 24 GHz radar sensor (IMST sentire sR-1200) implementation on a DJI Phantom 2 quadcopter for autonomous sea ice thickness and SWE mapping on a lake environment. However, the system showed comparatively poor performance when used without an adjacent metallic plate for radar-based ground detection and flight heights were limited to a few meters, making the system unsuitable for large scale, high resolution snow mapping.

Nevertheless, the most robust and reliable SWE products over larger areas right now are still not directly measured, but rather merged from direct snow depth measurements and some kind of physical snow model[7,13,16] or advanced machine learning algorithms.[14,26] The idea behind this concept is that the majority of spatial and temporal SWE variation comes from changes of snow depth rather than snow density.[13] In fact, typical seasonal snow densities comprise only a rather narrow spectrum, ranging from 30–120 $kg/m^3$ for fresh snow[27,28] to at most 550 $kg/m^3$ at the end of a season.[29,30] For comparison, snow depth variations throughout a season typically exhibit dynamic ranges $\geq 4$ times as large as that of snow density.[13] The ASO (as described in section 2.1), for example, does not only deliver spatial snow depth maps, but also a SWE estimate based on a physically-based energy-balance snowmelt model called *iSNOBAL*.[7,31] This model takes several input variables such as incoming thermal radiation, precipitation mass, air temperature, etc. and gives, amongst others, snow density as an output variable. Typical errors of SWE compared to field measurements range between 5–20 %. Other concepts try to circumvent the need of using external physical parameters, e.g. by using semi-empirical models such as applying the rules of snow compaction by Newtonian viscosity to a snowpack as published recently by Winkler et al.[16] Due to this, the only parameter needed is a time series of snow depth measurements and SWE errors were comparable to those acquired from other, more sophisticated thermodynamic snow models.

At the moment, one of the most rapidly emerging research sectors in data science for sure is the field of machine learning. Recently, even into snow sciences machine learning has found its way in terms of being used for machine-learning-based SWE determination. Broxton et al. presented intriguing data collected in Arizona (USA) where they associated local snow density measurements (measured within framework of the SNOTEL sensor network) in the field with geophysical attributes such as elevation, slope, northness, canopy closure and canopy height.[14] With these data an artificial neural network was trained and applied to two large-scale airborne LiDAR data sets during midwinter and late-winter. As a result, they demonstrated that depending on the season the representativeness of local SWE point measurements can vary by up to 30 %. These findings point out the necessity of either very well-distributed and representative sensor network systems or, more importantly, the need of high spatial resolution, remotely sensed SWE maps independent of local measurements.

When comparing these methods for remote sensing of snow depth and SWE, it is apparent that each of these techniques has some drawbacks and there is still a lot of room for improvement. For example, TLS measurements are limited by accessibility of regions with the quite bulky equipment or obstacles in the line of sight.[9] But also state of the art airborne measurements methods like the ALS have to deal with several drawbacks, e.g. operational costs being very high. In addition, safety requirements require the plane to fly at a fixed altitude above mountainous regions, resulting in largely varying LiDAR footprint sizes in the resulting maps and, hence, lost spatial resolution.[5] Hence, there is a huge demand within the environmental science and snow hydrology community for more flexible, affordable and accurate mapping solutions than the ones already existing. To our best knowledge, in literature there is no publication available reporting on a compact UAV-based multispectral LiDAR sensor for concurrent snow depth and water content mapping, as described in this publication.

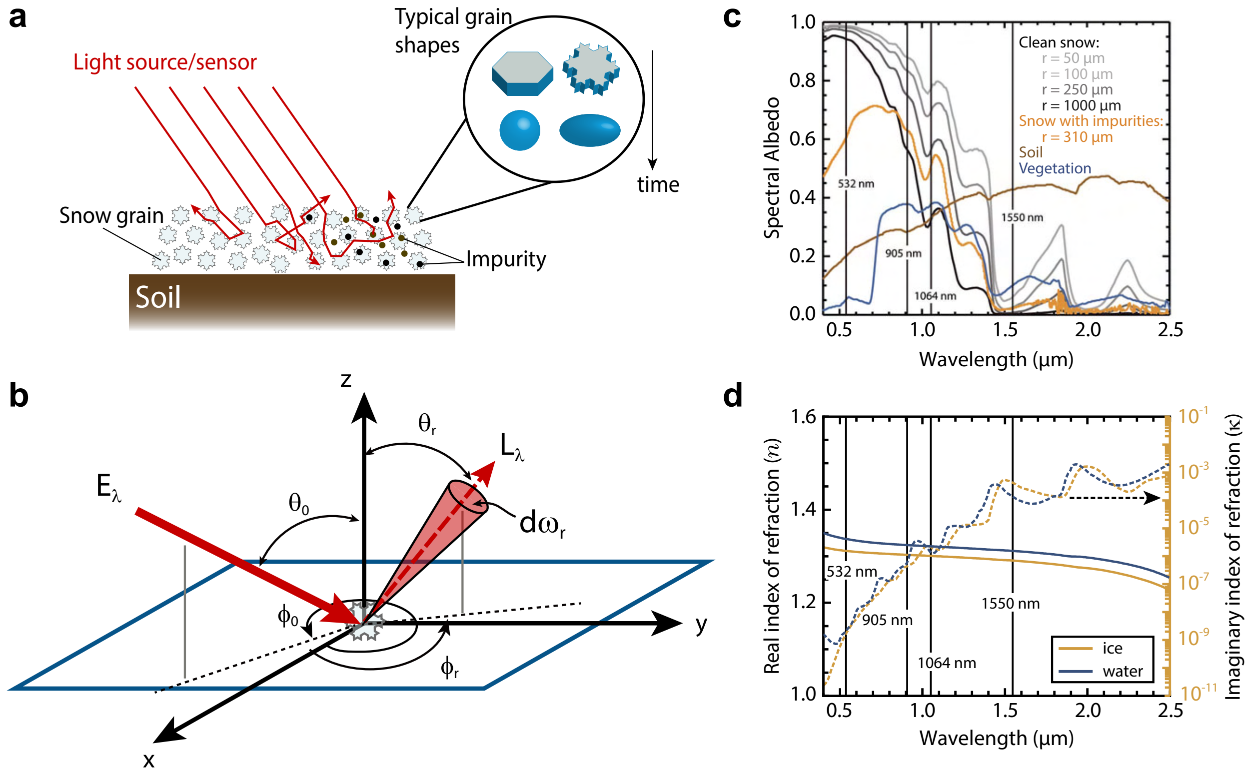


Figure 2: **a**, typical processes involved in light-snow interaction including single scattering, multiple scattering, ice absorption and absorption by impurities. Adapted from He and Flanner.[32] **b**, representation of the BRDF and definition of related variables. Inset: typical examples of grain shapes. As snow grains age, they tend to become more and more spherical. **c**, spectral albedo of snow simulated for varying grain sizes (grey/black) and in the presence of impurities (orange). Spectral albedos of soil (brown) and vegetation (blue) are included for comparison. Taken from Deems et al.[6] **d**, real (left axis) and imaginary (right axis) index of refraction of ice and water. Data taken from Segelstein[33] and Warren and Brandt.[34]

# 3. CONCEPT FOR MULTISPECTRAL SENSING OF SNOW DEPTH AND WATER CONTENT

## 3.1 Theoretical Background

In order to understand our proposed multiwavelength approach for measuring snow surface properties such as snow grain size, it is important to be familiar with the fundamental optical properties of the medium snow. This section gives an overview of the most important optical properties of snow that should be taken into account, but for a deeper understanding the reader should consult some of the cited publications.

Objectively speaking, the optical medium snow in its pure form basically consists only of ice particles and air as illustrated in Fig. 2a. In this publication, we limit our considerations to the case of a snowpack on a Lambertian surface, i.e., snow overlying the ground. In this case, the main processes involved in light scattering in snow are single- and multiple-scattering events of photons along with moderate absorption in clean snow, and stronger absorption due to impurities in dirty snow (Fig. 2a). Theoretical snow optics tries to simulate and quantify these processes using a variety of different snow models. Especially for remote sensing techniques like LiDAR, so-called bidirectional reflectance distribution function (BRDF) is of fundamental importance.[35] Following Nicodemus et al., this function for a given wavelength $\lambda$ is defined as:[36]

$$\mathrm{BRDF}_\lambda(\theta_0, \phi_0; \theta_\mathrm{r}, \phi_\mathrm{r}) = \frac{\mathrm{d}L_\lambda(\theta_\mathrm{r}, \phi_\mathrm{r})}{\mu_0\, \mathrm{d}E_\lambda(\theta_0, \phi_0)} \left[\mathrm{sr}^{-1}\right]. \tag{2}$$

The BRDF simply describes the relationship between incoming direct irradiance $E_\lambda(\theta_0, \phi_0)$ $[\mathrm{W} \cdot \mathrm{m}^{-2}]$ and reflected radiance $L_\lambda(\theta_\mathrm{r}, \phi_\mathrm{r})$ $[\mathrm{W} \cdot \mathrm{m}^{-2} \cdot \mathrm{sr}^{-1}]$ as shown in Fig. 2b, where $\mu_0 = \cos\theta_0$. $\theta_0$, $\phi_0$, $\theta_\mathrm{r}$, $\phi_\mathrm{r}$ are the zenith and azimuth angles of the incoming and reflected intensity, respectively. The received intensity of an airborne LiDAR sensor then would be determined by $\mathrm{BRDF}_\lambda(\theta_0, \phi_0; \theta_\mathrm{r} = \theta_0, \phi_\mathrm{r} = \phi_0)$. Note that a real sensor will never be able to measure solely the infinitesimal reflected radiance $L_\lambda$, but rather an average value over a solid angle $\mathrm{d}\omega_\mathrm{r}$ as indicated by the red shaded cone in Fig. 2b.

Another quantity describing snow optical properties and being discussed in literature even more thoroughly is the spectral directional-hemispherical reflectance, or short albedo $a_\lambda(\theta_0)$. The albedo is the ratio of the reflected flux of a surface to the total incident direct illumination, i.e. the integral of eq. (2) over all reflection angles.[37] A common approach used in snow optics to determine $a_\lambda$ is to model the snowpack as a plane-parallel homogeneous medium and solving the radiative transfer equation for this geometry.[32] One of the earliest and most accurate solutions to this equation was reported by Wiscombe and Warren in 1980.[38]

### 3.1.1 Impact of Grain Size on Snow Reflectance

Using their model $a_\lambda$ can be calculated as a function of snowpack depth, solar zenith angle, underlying albedo of the ground, ratio of direct-to-diffuse radiation and, importantly, grain size of pure snow using so-called delta-Eddington approximation. Within their framework Wiscombe and Warren modeled the ice grains as spheres and the snow reflectance as a multiple scattering problem. In case of snow, the typical effective particle radius is much larger than the wavelength of radiation of the solar spectrum. Therefore, single ice grain scattering can assumed to be governed by Mie scattering with ice grains acting as isolated scatterers.[38–40] The parameters required for describing this Mie scattering are the extinction efficiency $Q_\mathrm{ext}$ (i.e. the sum of scattering and absorption efficiencies), single scattering albedo $\tilde{\omega}$ (i.e. the probability of a photon to be scattered and not absorbed) and the asymmetry factor $g$ (i.e. the quantity describing the type of scattering with $-1 \leq g \leq +1$ corresponding to complete forward/back-scattering for $g = +/-1$ and isotropic scattering for $g = 0$).[37] Fig. 2c displays the results calculated for grain sizes ranging from 50 µm (light gray) to 1000 µm (dark gray) (adapted from Deems et al.[6]). These grain sizes correspond to those typically observed in field measurements: Grain sizes of fresh snow range from 20–100 µm and tend to increase through environmental processes such as melting-and-freezing cycles to around 100–300 µm. Older snow, i.e. commonly snow prevailing one or more seasons, might even reach sizes of 1.0–1.5 mm.[38] The simulated spectral albedo demonstrates the intriguing optical properties of snow very intuitively: In the visible range of the electromagnetic spectrum snow is highly reflective with spectral albedo near unity. This matches everybody's personal visual perception of snow being a white, strongly reflecting medium, especially when compared to other media such as vegetation or soil (depicted in blue and brown, respectively).

However, with increasing wavelength snow albedo drops drastically and even reaches a minimum near zero around 1500 nm. Although this tendency can be observed for all grain sizes, it gets pronounced more prominently for larger grain sizes. On a microscopic scale, this observation can be understood in simplistic manner: each scattering process of a photon happens at the ice-air interface of an ice grain, whereas photon absorption occurs during transitioning through the grain. This implies that when grain size increases, the optical path through an ice grain increases as well, resulting in less probability of scattering and higher absorption.[37] The decrease in albedo with increasing grain size is a very important observation because it provides a measure to infer snow grain sizes from spectroscopic measurements and is the fundamental idea behind our measurement approach. Also in literature many groups used this property of snow to determine the size of snow grains remotely.[41–45] Nevertheless, most of the data available in literature is based on passively sensed spectral data from satellite (e.g. Dozier et al.[44]) or airborne platforms (e.g. Nolin and Dozier[41]). In particular, none of them combines LiDAR snow depth mapping with co-registered information of the snowpack's grain size distribution in a single compact sensor system.

### 3.1.2 Impact of Liquid Water on Snow Reflectance

Naively spoken, the most straight forward way of sensing the presence of liquid water in a snowpack would be by its direct impact on albedo or reflectance. In general, the optical properties of a medium are governed by its (complex) index of refraction $\tilde{n}$:

$$\tilde{n} = n + i\kappa \tag{3}$$

The real part $n$ describes refraction and the imaginary part $\kappa$ determines the absorption. Fig. 2d shows both, $\tilde{n}_{\text{water}}$ (taken from Segelstein[33]) in blue and $\tilde{n}_{\text{ice}}$ (taken from Warren and Brandt[34]) in yellow for the spectral range from 400 nm to 2.5 µm. Comparing both, it gets obvious that for the relevant spectral range there are only subtle differences between the two of them: the real index of refraction only shows slight variability over the whole range in general, but differences between ice and water reamin insignificant. Contrarily, the imaginary index of refraction varies for both media over at least six orders of magnitude, from moderately absorptive in the visible range to strong absorption in the near infrared. When comparing this property to spectral albedo in Fig. 2c it can be seen that the decrease of albedo at larger wavelengths is directly connected to the increasing imaginary index of refraction of the ice grains. Although there is a strong resemblance between the refractive indices of ice and water, some local extrema are slightly shifted towards shorter wavelengths. Green et al.[45] exploited this shift of local minimum in albedo from 1030 nm towards smaller wavelengths to derive the melting status of a snowpack.

However, measurements by O'Brien and Munis of melting snow clearly showed that albedo decreases at the presence of liquid water.[46] Wiscombe and Warren argued that this observation is due to liquid water replacing the air between ice grains, effectively increasing the effective grain size rather than due to the liquid water itself.[38] This explanation is further supported by further spectral albedo measurements of a fresh snow sample before and after hot air had been blown over the surface. When liquid water was present, the albedo decreased. But after refreezing again, albedo remained unchanged, excluding the mere presence of liquid water being the reason.[46] Hence, even though the presence of liquid water itself does not alter the general spectral properties of the snowpack significantly, the albedo decreases due to an effective increase in grain size. For completeness it should be mentioned that under normal circumstances the liquid water fraction in a snowpack barely exceeds 5–6 %, which is no significant amount to alter the bulk optical properties solely due to the mere presence of liquid water.[47]

### 3.1.3 Impact of Snow Density on Snow Reflectance

Following the measurements by O'Brien and Munis, in a very similar manner it might be argued that there is a dependence of snow albedo on density (e.g. Fig. 6 of O'Brien and Munis[46]). In spite of that, none of all accurate snow optics models used during the last decades by the snow science community contains an explicit dependency on snow density. Rather than density itself, again, it is the grain size which is interpreted to lead to these observations. In a simple experiment Bohren and Beschta separated those two variables and their contribution on snow albedo measuring a snow sample once in a fresh state and once after compacting it artificially, keeping snow grain size constant. In both cases, the measured albedo was the same within a few percent uncertainty, ruling out density itself being the reason.[48] Consequently, two snowpacks of different densities, but identical SWE (i.e. the two snowpacks must have different snow depths) would show the same reflectance, given an identical grain size distribution in both snowpacks.

For a fresh snowpack this means that, as it ages, melting and freezing cycles during a season lead to wet snow metamorphism, i.e. a clustering of surface ice crystals. Consequently, the effective grain size increases, resulting in decreasing albedo.[37,38,45,49] Characteristic snow densities measured in the field range from 30–120 $\text{kg} \cdot \text{m}^{-3}$ for fresh snow to 200–500 $\text{kg} \cdot \text{m}^{-3}$ at the end of a season and rarely exceed 550 $\text{kg} \cdot \text{m}^{-3}$.[23] On the other hand, it was predicted that only for densities exceeding values around 650 $\text{kg} \cdot \text{m}^{-3}$ density-related near-field effects start influencing snow optical properties[47] – far more than regular snow densities.

In spite of these properties, also the depth of light penetration into the snowpack has to be considered at this point. Even though snow density has no direct impact on albedo, there is a proportionality between particle number density and optical depth of a snowpack, i.e. the measure to what extent electromagnetic radiation can penetrate into a snowpack. As a direct consequence, the penetration depth into a layer of larger particles exceeds that for smaller particles, since at a constant bulk density the particle density is smaller.[42] In general, maximum light penetration into snow is restricted only to the upper $\sim 10$ cm in the visible range ($\sim 532$ nm) and to a few cm in the near infrared ($\gtrsim 900$ nm).[6,50] For any spectroscopic measurement of snow parameters in the visible or near-infrared this means that only the first few cm of a snowpack can be characterized and not the bulk. In this range, however, snow density can be assumed to be constant, simplifying the interpretation of snow parameter retrievals such as grain size.[41]

### 3.1.4 Anisotropic Scattering of Snow

Up to now, we only considered the directionless snow albedo for a fundamental understanding of snow optical properties. As already mentioned before, quantitative snow properties retrievals using active remote sensing techniques such as LiDAR, however, require knowledge about both the spectral and angular directional reflectance of snow, expressed as BRDF (eq. (2)).

In fact, snow is a strongly forward-scattering medium. In the visible range the asymmetry parameter $g \approx 0.88$ and increases monotonously with increasing wavelength.[51] Hence, this means that the proportion of forwardly scattered intensity increases with wavelength. A similar tendency is observed with increasing grain size.[6,37] As a result, these effects can lead to substantial over or underestimations of remotely sensed snow parameters such as grain size, sub-pixel snow-covered area or spectral albedo depending on view angles or solar zenith angle.[52] In contrast to snow albedo, BRDF cannot be modeled using the early models by Warren and Wiscombe (cf. section 3.1.1) because these models only account for fluxes and not intensities. However, this problem was solved introducing a numerically stable implementation of the discrete ordinate radiative transfer (DISORT) method for solving the radiative transfer equation as reported by Stamnes et al.[53] This method is still often used as a benchmark for evaluating many problems in snow science.[32] For the computation of angular intensity distribution, it takes the whole single particle phase function $P(\Omega_1, \Omega_2)$ (i.e. the function describing the angular scattering probability of an incident photon with angle $\Omega_1 = (\theta_1, \phi_1)$ to angle $\Omega_2 = (\theta_2, \phi_2)$) as an input, instead of the asymmetry factor $g$, the mean cosine value.

The most comprehensive field study investigating the anisotropic snow scattering characteristic was reported by Painter and Dozier. They conducted high angular resolution measurements of the hemispherical-directional reflectance factor (HDRF), i.e. the BRDF including additionally diffuse irradiation, for different grain sizes and solar zenith angles and compared their results to a theoretical model computed using DISORT code.[54] Results demonstrated in a consistent manner that the scattering anisotropy int the forward direction increases significantly for near-infrared wavelengths compared to the visible regime. This happens due to two effects: First, as already mentioned, at longer wavelengths absorption is greater. Second, whereas at short wavelengths multiple-scattering dominates, the contribution of single scattering to the total reflected intensity increases with wavelength – leading to the observed behavior. Consistently, also for the larger grain sizes the overall observed HDRF intensities were greater compared to those corresponding to smaller grain sizes. As grain size increases, single-scattering coalbedo $(1 - \tilde{\omega})$ (absorption) rises (cf. Sec. 3.1.1) and also asymmetry parameter $g$ increases likewise, scattering photons even deeper into the snowpack.

As a direct consequence of these anisotropic scattering effects, special care has to be taken when interpreting any LiDAR mapping data of snow (single-wavelength or multi-spectral). Hence, several external parameters such as local topography, snow texture, surface roughness or liquid water content potentially introduce additional error sources, e.g. affecting the vertical error budget through time-walk effects.[6]

### 3.1.5 Impact of Irregular Snow grain Shape on Snow Reflectance

Although the assumption of spherical grains in optical snow models might deliver reasonable results for surface albedo, nonetheless, in reality the situation can be slightly more complex. First of all, snow flakes appear in a variety of different shapes following a complex growth morphology dependence on temperature and supersaturation.[55] Under normal atmospheric conditions, with decreasing temperature below $-2\,^{\circ}$C snow crystals tend to grow into thin plates, slim and hollow columns from $\sim -5\,^{\circ}$C to $-10\,^{\circ}$C and around $-15\,^{\circ}$C into thin plates again. As a rule of thumb, as supersaturation increases, morphological complexity also increases for all temperatures, resulting for some cases in the well-known hexagonal snowflake shape depicted in the inset of Fig. 2a.[55,56]

Leroux et al. implemented a first model including not only spherical grains, but also hexagonally shaped grains based on the adding/doubling method and compared their results to field measurements of BRDF.[57,58] In their study, indeed, only hexagonal grains could describe the BRDF and also snow grain size variations satisfactorily. Kokhanovsky et al. further developed a more realistic model of snow optics modelling snow grains as fractal close-packed ice grains, describing scattering by simple geometrical optics equations and finding an analytical, asymptotic solution to the radiative transfer equation.[59] They could demonstrate that grain size estimates based on a fractal model lead to $\sim 40\,\%$ larger values compared to the spherical model. Similar discrepancies were observed in prior studies comparing remotely sensed grain sizes retrievals to field measurements.[60,61] Physically speaking, non-spherical snow grains have up to $\sim 20\,\%$ smaller asymmetry factors $g$ and, thus, show less forward-scattering than their spherical counterparts.[32,62]

#### 3.1.6 Impact of Impurities on Snow Reflectance

Besides snow grain size and shape, snow reflectance is also fundamentally affected by impurities like dust or soot (black carbon) in snow.[5,37,63] In contrast to grain size, which affects primarily near-infrared reflectance, an increasing impurity concentration reduces visible light reflectance.[62–65] This can be seen in the orange curve in Fig. 2c. Nevertheless, grain size and shape still influence single-scattering coalbedo, i.e. also snow reflectance. Therefore, for varying grain sizes the same impurity concentration can lead to varying absolute reflectance values.

#### 3.1.7 Impact of Shallow Snow depths on Snow Reflectance

For completeness, at this point also the impact of shallow snow depths on snow reflectance shall be mentioned. All considerations before were based on assuming the snowpack to behave as an optically semi-infinite medium. As discussed in Sec. 3.1.3 light penetration into a snowpack is restricted to $\lesssim$10–20 cm in the visible regime and only a few cm for near-infrared wavelengths. Due to this, shallow snowpacks below 20 cm can exhibit some counter-intuitive optical response. Since the optical depth is inversely depending on grain radius $r$, this means that a shallow snowpack might become optically finite as the snow ages (i.e. grain size increases) whereas a thicker snowpack remains optically semi-infinite, even though their grain sizes evolution would be exactly identical.[38] As a direct result, the underlying surface would start to "shine through" the snow surface, unexpectedly altering snow albedo and reflectance and opening a potential source of erroneous snow parameter inferences.

### 3.2 Proposal for a Multispectral LiDAR Snow Sensor

Putting these characteristics together, we propose the following approach for a simultaneous snow depth and water content mapping sensor: Our novel snow mapping sensor will operate as a multispectral pulse-time-of-flight[66] LiDAR scanner with two wavelengths - one in the visible range of the electromagnetic spectrum at 515 nm and one in the near-infrared regime at 1030 nm. For each of these wavelengths the distance $D$ between the scanner and the snowpack, can be determined by measuring the round-trip time interval $\Delta t_\mathrm{r}$, i.e. the period of time a pulse needs to propagate from the scanner to the target and back, via

$$D = \frac{v_\mathrm{g} \cdot \Delta t_\mathrm{r}}{2} \tag{4}$$

Here, $v_\mathrm{g}$ denotes the group velocity of light in the atmosphere. Apart from the pure distance information, due to the two different wavelengths every single distance measurement also contains additional information about the snow grain size of the snowpack at the same spot. It was discussed in Sec. 3.1.1 that snow albedo is highest in the visible range with values close to unity, but rather insensitive to changes in effective grain size of the snowpack (cf. Fig. 2c). Contrarily, in the near-infrared regime albedo decreases as the effective grain size increases. Hence, by comparing the intensities of the backscattered signal of the two wavelengths, in principle we can infer the effective grain size of the snowpack with a single measurement. These information can then be fed into state-of-the-art snow models such as SNOWPACK/ALPINE 3D[67] or FSM2[68] to deduce the local snow density $\rho_\mathrm{s}$ for each measurement and therefore, according to eq. (1), also SWE. Due to the finite penetration of light into the snowpack, however, only the size distribution of the upper few cm of the snowpack will be probed. This drawback can be overcome by frequent, multi-temporal measurements of the snowpack over the duration of a whole season.

Moreover, note that due to the non-linear processes involved in the Nd:YAG laser, our approach ensures that both pulses of differing wavelengths are always emitted at the exact same time and possess perfect coherence. This means that each measured data point always contains the multi-spectral information.

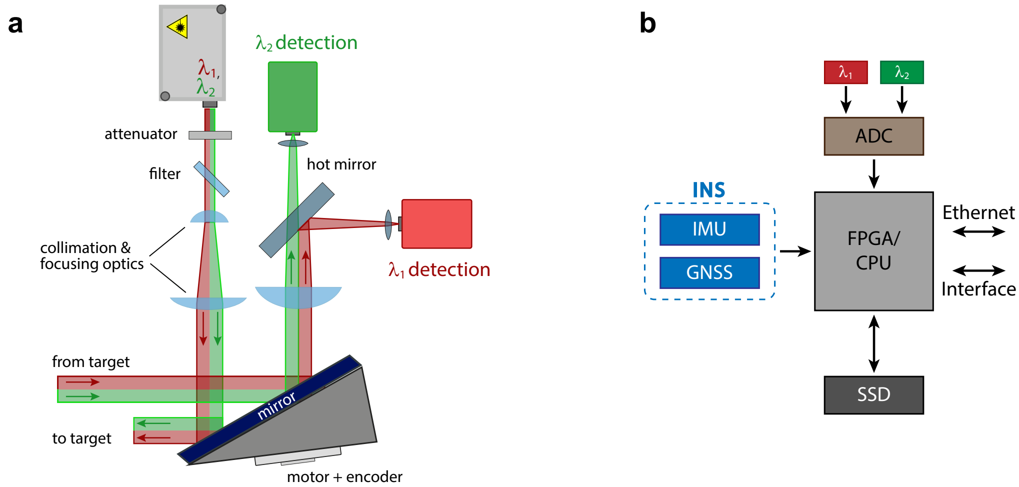


Figure 3: **a**, illustration of the proposed dual-wavelength LiDAR scanner layout. The laser source emits light at wavelengths $\lambda_1 = 1030\,\mathrm{nm}$ and $\lambda_2 = 515\,\mathrm{nm}$. For guaranteeing eye safety, the beam is widened up by a telescope beam expander setup before hitting the scan mirror. In the receiving unit the back-scattered light is spectrally separated by a hot mirror and registered by the respective detector. **b**, reduced electronic block diagram of the setup. The received light signal is digitized as full-waveform signal using a high-performance FPGA board and written to an SSD. At the same time, the FPGA communicates with the external INS and stores the sensor's position and attitude for later geo-referencing of the data.

### 3.2.1 Technical Realization

In Fig. 3a you can see the schematics of our proposed lightweight LiDAR sensor setup. At the heart of our system we implement a passively Q-switched, ultra-compact Nd:YAG laser emitting ns-pulses at both its fundamental and frequency doubled wavelengths $\lambda_1 = 1030\,\mathrm{nm}$ and $\lambda_2 = 515\,\mathrm{nm}$ with a repetition rate of 10 kHz. Since the system shall be used in public space, special care has to be taken into account for guaranteeing eye safety. To achieve this, the outgoing laser beam diameter is expanded using a telescope beam expander setup as illustrated in Fig. 3a. A rotating planar mirror mounted behind at an angle of 45° with respect to the beam axis then is used to scan the beam over the area of interest.

After being backreflected, the signal is collected by the detection arm of the system and the two wavelengths are separated spatially by a hot mirror to be detected with their individual photon detectors; the hot mirror lets the 515 nm signal pass, while it reflects the 1030 nm.

Many conventional LiDAR sensors only detect a single or a limited number of discrete return in a single measurement which are then stored as distance information. Our proposed system instead will be able to record the whole waveform of the backscattered signal at fine temporal resolution with a sampling rate of 4 GbPS, enabling so-called full-waveform-analysis.[69] Obviously, handling and processing these high data rates demand special attention to be integrated into a small form factor device. We plan to address this issue employing a high-performance field-programmable gate array (FPGA) with integrated CPU as the central element of our measurement electronics. The FPGA receives the received signal from the analog-to-digital converter (ADC) and writes them to en external solid-state drive (SSD). Asides from handling the measured data, the FPGA also acts as central controller and communication unit for the other system components such as the scanning motor and encoder, or the external GNSS positioning solution (Fig. 3b). The huge benefit of the full-waveform analysis is illustrated in Fig. 4. A laser pulse emitted from the LiDAR sensor has a finite probability to partially penetrate a tree canopy and, finally, even to hit the ground and being backreflected to the sensor. This is already a huge advantage of LiDAR itself over other techniques such as SfM because it allows for precise snow height mapping even under conditions like a canopy covering the ground.[8,11,12] This advantage of full-waveform recording is illustrated in the panel on the right. The full-waveform signal provides additional information on parameters like canopy height or structure. As outlined above, the measured difference in relative intensity $\Delta I$ then can be attributed to a certain grain size of the snow layers. Referring back to effects of shallow snowpacks discussed in Sec. 3.1.7, it might also be possible in principle to tell from the backscattered signal whether the canopy itself is covered with a thick or thin snow layer, or even not all.

In a second step single LiDAR scans have to be transformed into a point cloud. To realize this, the compact and lightweight design of the system will allow the sensor to be mounted to a UAV which can be used to map a larger area in a single data acquisition. However, for acquiring meaningful hydrological data, high resolution mapping of the snowpack depth over a season will require a geo-referenced point cloud with a spatial accuracy and precision on the cm range. For this reason the sensor will be equipped with a high-end INS (e.g. APX-15) positioning solution. Using enhanced post-processing techniques like differential GNSS (DGNSS) the modern INS can yield a typical positional root-mean-square (RMS) error of 2–5 cm; the integrated MEMS-based inertial sensor provides a post-processed RMS error of 0.025° on roll and pitch angles, and 0.080° RMS error on the true heading, respectively. These characteristics will provide a basis for producing high resolution multispectral LiDAR maps of a snow cover, opening the door to a completely new field of snow remote sensing techniques.

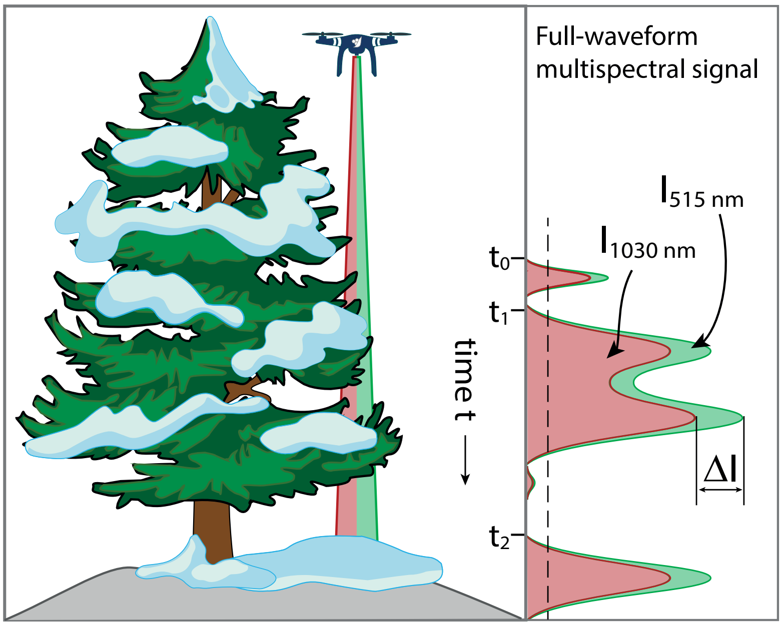


Figure 4: Illustration of the proposed measurement principle and advantage of full-waveform LiDAR signal recording. For each emitted pulse there is a finite probability that a portion of the pulse penetrates the canopy and gets potentially reflected back from the ground to the sensor. Backreflections in between, e.g. from different canopy levels, are visible in the full-waveform recorded signal. During post-processing, the difference in intensity between the visible and near-infrared channel $\Delta I$ can be translated to a certain grain size and SWE. After Lefsky et al.[70]

### 3.3 Conceptual Tests of LiDAR Snow Depth Measurements

In order to gain a first understanding of measuring snow depth using LiDAR before developing a home-built system, we carried out first field experiments with a commercially available LiDAR sensor. Given the spectral reflectance of snow (Fig. 2c) and the availability of commercial LiDAR systems, we chose a Velodyne VLP-16 for our tests. With an operating wavelength of 903 nm and its low weight of $\sim$ 590 g it provides a decent trade-off between spectral reflectance of snow at this wavelength and a low weight for later integration to a UAV platform. In addition, the potential usage on a UAV is supported by its maximum measurement range of 100 m and the usage of 16 laser lines opening up a ±15° vertical field of view angle at 360° azimuth angle coverage.

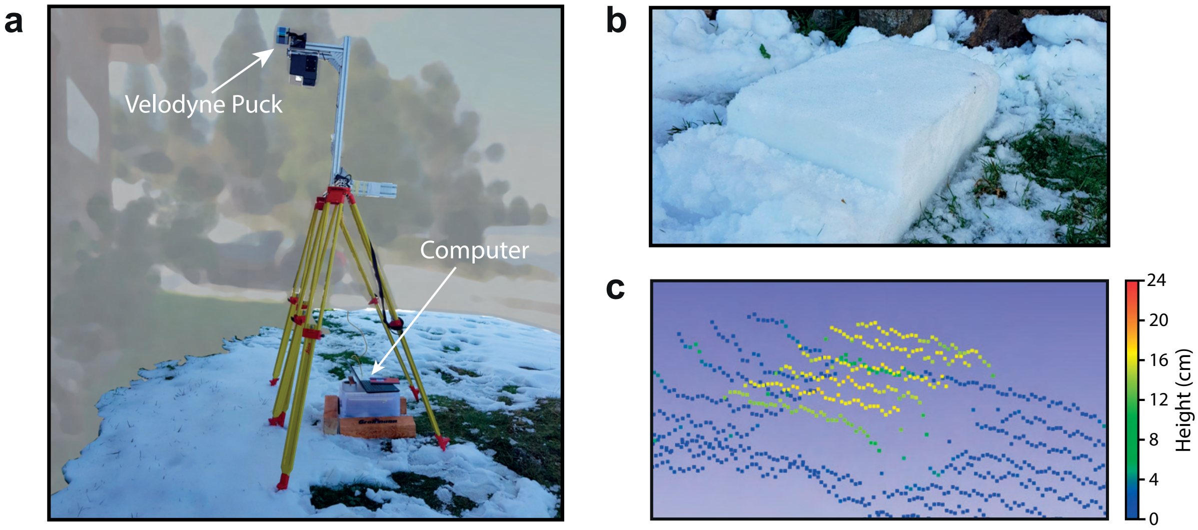


Figure 5: Conceptual snow height measurements with a Veoldyne Puck VLP-16. **a**, measurement setup. **b**, photograph of an 18 cm snow block. **c**, the corresponding point cloud of the snow block shown in **b**. The absolute height of each data point with respect to the ground measured without snow is color-coded according to the scale shown.

In a first simplistic experiment we evaluated the applicability of the VLP-16 for snow depth measurements in general. For doing so, we mounted the sensor at a height of $\sim 2.6$ m above a snow surface as depicted in Fig. 5a. It can be seen in the photograph that the natural snow layer was quite thin, which is why we created artificial snow blocks with heights of 13 cm, 18 cm and 24 cm in order to compare measurements of different snowpack heights. The 18 cm snow block is shown as an example in Fig. 5b. For each of these snow blocks then a point cloud was acquired and its height was determined by calculating the difference between the point cloud and a reference point cloud acquired without any snow. Fig. 5c displays the resulting point cloud for the snow block shown in b. According to the central limit theorem, the height values follow a normal distribution[71] so that the height can be determined by fitting a normal distribution to the height value histogram. Instead of 13 cm, 18 cm and 24 cm we extracted heights of $(11.4 \pm 1.3)$ cm, $(15.2 \pm 1.7)$ cm and $(23.1 \pm 1.3)$ cm, respectively. Hence, we conclude that the VLP-16 tends to underestimate the actual snow height. Still,these results demonstrate that – within the accuracy range of $\pm 3$ cm stated for the VLP-16[72] and confirmed elsewhere[73,74] – the snow block heights measured by the LiDAR agree well with the reference values measured by hand with a ruler. Anyways, for integration into a UAV platform this observed tendency of underestimating snow depth has to be taken into account when analyzing the total error budget of the system. Most common error sources generally comprise GNSS positioning, terrain- and vegetation-induced or post-processing errors, all of which can be up to several cm.

To further understand the reflected LiDAR intensity of a snow cover, we compared the received intensity by the VLP-16 LiDAR sensor in more detail for a shallow 3 cm snow cover (Fig. 6a) and bare grass lawn (Fig. 6b) to a thicker snow cover of 7 cm. Note that for these tests we restricted our focus on $\pm 20°$ azimuth angle and $-3$–$15°$ vertical angle. At this point it is also worth noting that the VLP-16 assigns values from 0 to 100 for reflectivities from 0 to 100 % of a standard diffuse reflector to the received intensity. The absolute intensity difference of the two situations displayed in Fig. 6a and b with respect to the undisturbed snow surface can be found in the upper and lower panels in Fig. 6c, respectively. These simple measurements demonstrate the strong dependence of light penetration depth on wavelength: In the photograph of the shallow 3 cm snow cover (Fig. 6a) the underlying grass lawn surface already starts being visible through the snow surface. Although for some data points in the corresponding intensity plot in Fig. 6c a $\sim 40$ % smaller intensity was measured, the overall intensity in the area of the shallow snow cover did not change significantly. This demonstrates that at 903 nm wavelength, the 3 cm

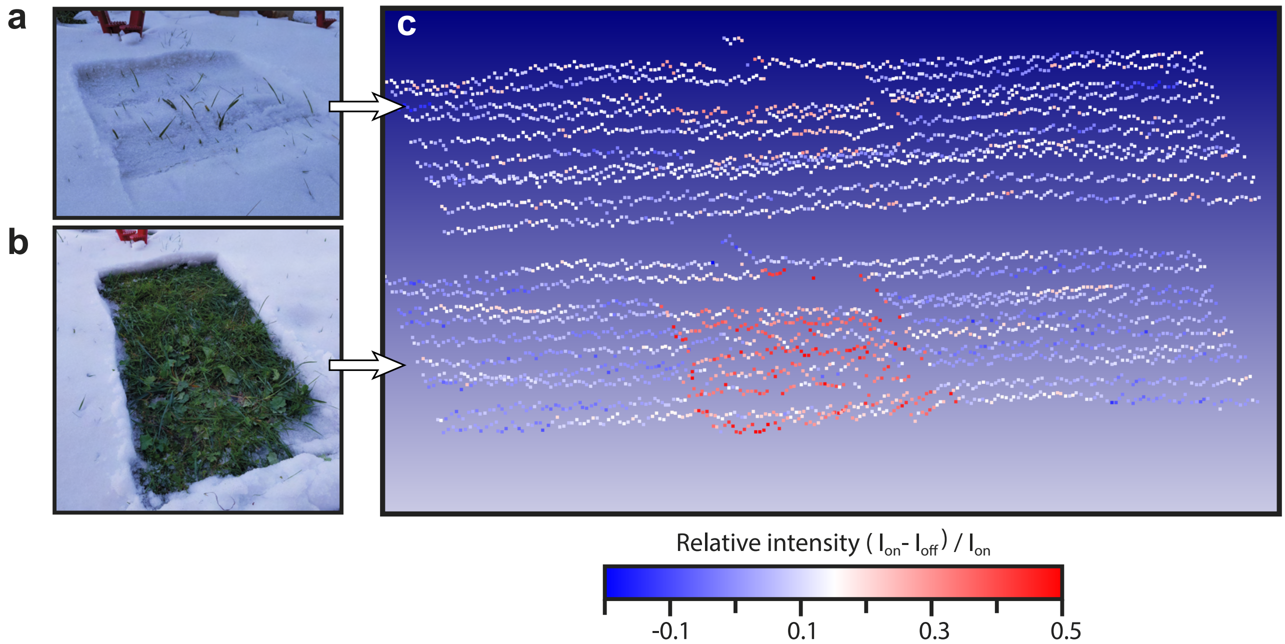

Figure 6: Intensity measurements of shallow snow. **a**, photograph of a shallow snow pit of $\sim 3$ cm depth. The undisturbed snow had a depth of 7 cm. **b**, the same spot as in **a**, but with snow removed completely in the area of the snow pit. **c,** corresponding point clouds to **a** and **b** with color-coded intensity difference $I_{\mathrm{on}} - I_{\mathrm{off}}$ normalized to the intensity of undisturbed snow surface $I_{\mathrm{on}}$. In case of the shallow snow depth of 3 cm, the snow cover remains mainly optically semi-infinite at the 903 nm wavelength of the VP-16, so no notable change in intensity was observed. As soon as the snow was removed, intensity dropped by up to 50 %.

shallow snow cover still acts as an optically semi-infinite surface. The remaining variation for single data points might be caused by single grass blades penetrating the snow surface or reflection effects at the edges of the snow pit. On the other hand, when removing the snow completely, received intensity dropped significantly by up to 50 % over the whole area where snow was removed (Fig. 6c, lower panel). Our observations are consistent with theoretical considerations for thin snow covers reported by Wiscombe and Warren[38,75] and experimental findings for temperate snow covers by Perovich.[50]

Regarding the snow depth in this experiment, however, the VLP-16 was not able to resolve the correct snow depth. In both cases shown in 6a and b the same snow depth was determined by subtracting snow on and snow off point clouds. One reason for this is that the grass lawn surface is not an even surface and as soon as snow was removed, the grass blades straightened up a few cm as it can be seen in 6b. The second reason might be due to the sensor measuring distances at its limit of accuracy, so that it could not resolve the shallo snow layer differences properly.

### 3.4 LiDAR Tests on a UAV Platform

In a next step, to carry out first airborne LiDAR measurements at a single wavelength, we mounted the VLP-16 to a vertical take-off and landing (VTOL) UAV platform as depicted in Fig. 7a. For this purpose we chose the Delta Quad Pro Cargo designed by Vertical Technologies providing flexible payload integration up to a maximum weight of 1.2 kg together with long flight times of up to 110 min. The Puck was installed into the fuselage so that a $\pm 45°$ cross-track field-of-view scan angle and $\pm 15°$ along-track view angle were realized. To make the system as lightweight as possible, the VLP-16 was controlled by a Raspberry Pi Zero single-board computer and powered using the primary on-board electronics power supply.

The data presented here were all captured during mid-winter season on January 20, 2021 in a mid elevation mountainside at Schauinsland near Freiburg (N 47.914 72°, E 7.909 91°, 1200 m above sea level). Fig. 7b shows a

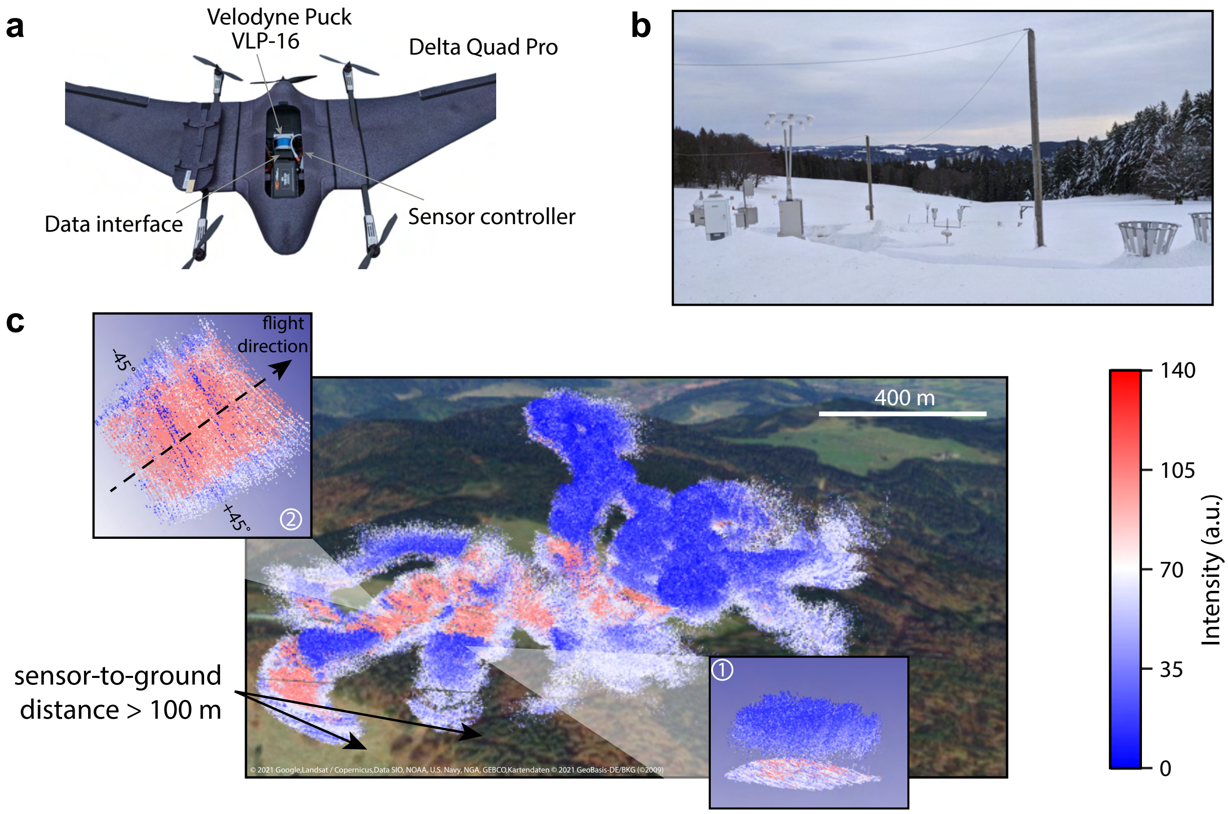


Figure 7: Airborne LiDAR mapping with the VLP-16. **a**, top view on the Delta Quad Pro VTOL used for point cloud acquisition. The VLP-16 sits flush with the curvature of the fuselage inside the payload bay, providing, $\pm 45°$ cross-track field-of-view and $\pm 15°$ along-track view angle. Lid open for illustrative purposes. **b**, snow conditions at the Schauinsland site on January, 2021. **c**, intensity-colored point cloud from a LiDAR survey on the same date. Inset No. 1: section of the point cloud showing typical canopy penetration capability of the VLP-16. Inset No. 2: typical across-track intensity dependence on view angle. At larger view angles, intensity drops significantly.

photograph of the site and the snow conditions on the same day of the survey.
LiDAR data acquisition was performed at a flight speed between 14 m/s and 28 m/s except for turning curves where speed could be slightly higher. The nominal altitude of the vehicle was 90 m above the launch site, but due to the hilly terrain the actual local altitudes above ground varied between 30 m and $>$ 100 m. We geo-referenced the resulting acquired LiDAR data using the on-board GNSS and IMU sensor data of the Delta Quad; the corresponding point cloud is shown in Fig. 7c. Although the quality of the GNSS/IMU data did not allow any quantitative evaluation of snow depth from this point cloud, the data still provides valuable information for future work. The first thing to be mentioned is the ground point density. It was already discussed that the huge advantage of LiDAR measurements over alternative passive methods is the potential of canopy penetration, so that also the terrain below the canopy can be mapped. This can be seen in inset No. 1 of Fig. 7c. The intensities measured below the canopy top, i.e. the forest ground, exhibit a similar average magnitude compared to the ones measured on the open field (inset No. 2). In contrast to this, the overall reflected intensity of the trees is significantly lower by a factor of up to 4. This clearly demonstrates the sensor's capabilities of canopy penetration and mapping of sub-canopy snow covers. Typical ground point densities extracted from our snow survey ranged from 12–37 points/m$^2$ in the forest and the open field, respectively. In a similar study, Jacobs et al. mounted the VLP-16 on a multicopter platform and reported ground point densities of 90 points/m$^2$ in the forest and 364 points/m$^2$ in the open field. These densities exceed ours by a factor of up to 10. However, flight parameters in the cited study were fundamentally different with much lower flight speeds of 7 m/s, as well as

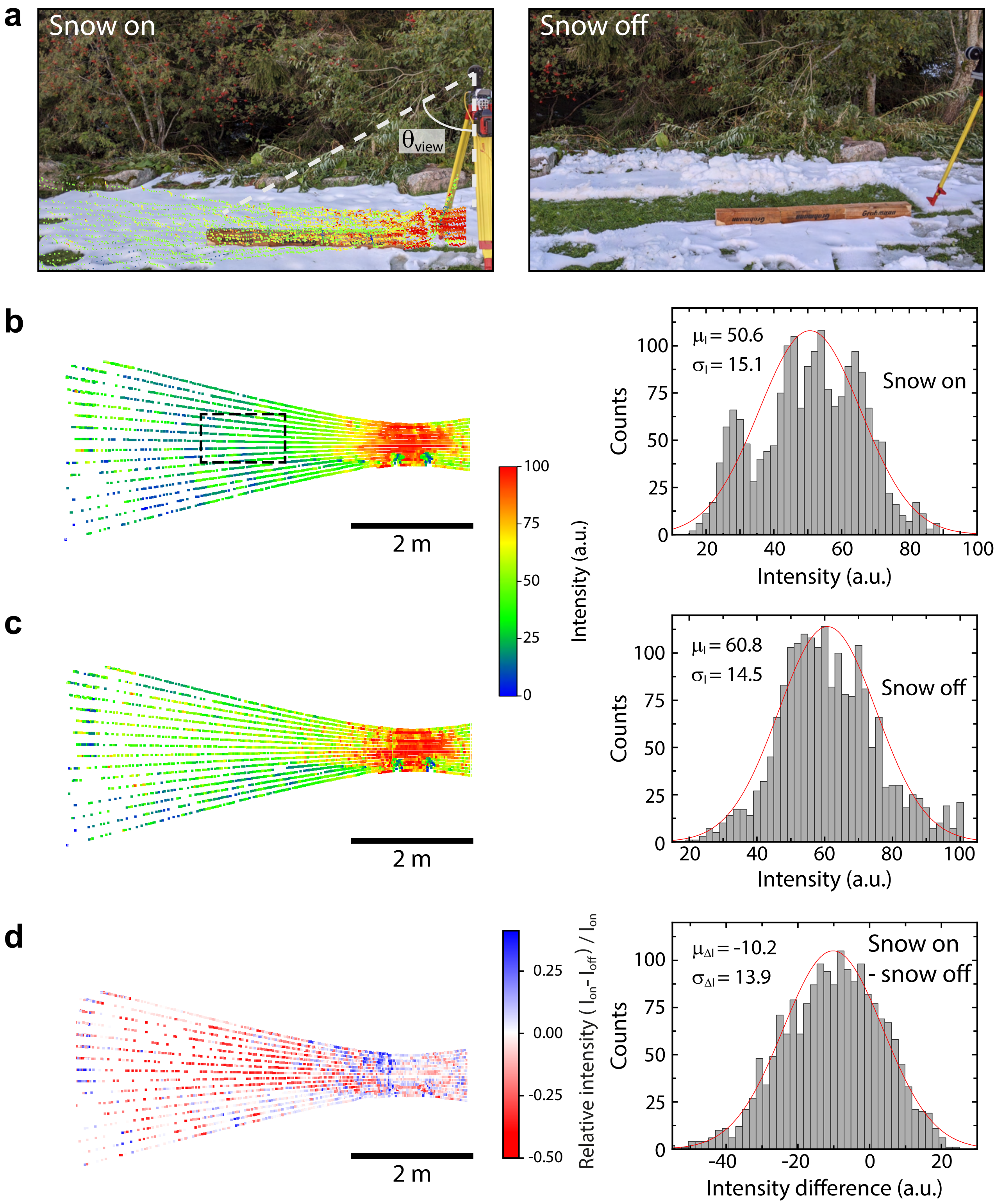


Figure 8: Detailed investigation of intensity dependence on view angle. **a**, photograph of the measurement setup for snow on (left) and snow off (right) conditions. **b**, top view on color-coded intensity snow on point cloud (left) and intensity histogram (right) of the area marked in the point cloud. A mean intensity value $\mu_I^{\text{snow on}} = 50.6$ was found. **c**, same as in **b**, but for snow off condition. Compared to **b**, at these larger view angles the histogram shows a larger mean intensity $\mu_I^{\text{snow off}} = 60.8$. **d**, $I_{\text{on}} - I_{\text{off}}$ intensity difference point cloud, normalized to $I_{\text{on}}$ (left) and matching histogram of the same area as in **b** (right). The intensity at larger view angles decreases stronger in case of the snow on condition due to the strongly forward-scattering characteristics of snow.

intentional 40 % overlap between flight lines. In addition, in our case we had to deal with hilly terrain, leading to varying ground point densities as well as voids in the point cloud where the distance between sensor and ground exceeded the maximum measuring distance of 100 m

The second important observation is the dependence of received back-scattered light intensity at large view angles as shown in inset No. 2. Obviously, back-scattered intensity drops significantly at larger view angles $\gtrsim 20°$. Although this behaviour might be expected qualitatively for other materials as well, in the case of snow it is even more pronounced. We could demonstrate this with a simple experiment measuring the reflected signal of a snow cover and grass lawn at a range of view angles. The corresponding setup for snow on and snow off conditions, as well as the definition of $\theta_{\text{view}}$ are depicted in Fig. 8a left and right panel, respectively. For both situations the intensity then was measured by the VLP-16 at different view angles; Fig. 8b and c (left panels) display a top-view of the measured intensity point clouds for the snow on and snow off situations. Fig. 8d shows the associated intensity difference point cloud between b and c. The panels on the right show an intensity histogram of the area highlighted by the dashed rectangle in Fig. 8b for each point cloud. The marked area covers a view angle range from ~35–65°. We determined the mean value in each case by fitting a normal distribution to the data. It is evident that the mean intensity in the highlighted area increases from $\mu_I = 50.6$ to $\mu_I = 60.8$ when the snow is removed. Consistently, also the intensity difference histogram is mainly normal distributed with a mean intensity difference of $\mu_{\Delta I} = \mu_I^{\text{snow on}} - \mu_I^{\text{snow off}} = -10.2$. The exact angle-dependent intensity for the measurements presented in Fig. 8 can be found in Fig. 9. It displays the averaged intensity of the upper eleven lines shown in Fig. 8b (snow on, blue curve) and c (snow off, red curve) at view angles from 0° to 70°. At smaller view angles $\lesssim 25°$ the high reflectance of snow dominates the magnitude of back-scattered intensity and the measured intensity on the snow on surface exceeds the corresponding intensity measured on the snow off surface; note that the dip in the red curve marked at $\sim 15°$ corresponds to edge between snow and grass covered areas. With increasing $\theta_{\text{view}}$, back-reflected intensity from the snow surface then decreases stronger than for the grass surface. These results demonstrate the forward-scattering behaviour of snow, leading to lower received intensity by a LiDAR sensor at larger view angles.

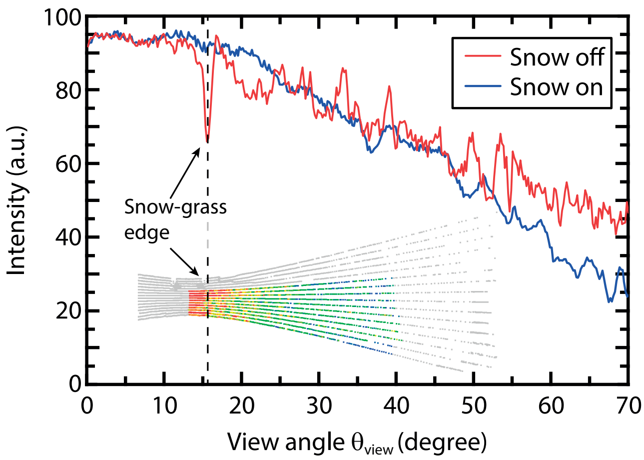


Figure 9: Detailed intensity dependence of reflected intensity on view angle from Fig. 8. The peak highlighted by the arrows corresponds to the edge between grass lawn and snow surface. For view angles $\theta_{\text{view}} \gtrsim 25°$ back-reflected intensity from the grass lawn exceeds the intensity from the snow surface.

## 4. FUTURE WORK

Based on the concept outlined above, until the next snow season a dual-wavelength LiDAR scanner will be built up on an already existing prototype platform. The system will then be mounted to a DJI M600 Pro multicopter and tested at the Schauinsland site described in the manuscript. Based on the results of these tests, the system will then be optimized regarding weight, footprint and optics design in order to increase the flight time of a single survey. A modified version of the system later might also be mounted to our Delta Quad VTOL vehicle to allow for even longer flight times and larger survey areas. However, this might require to get rid of heavy parts such as the rotating mirror, so that the system would not be a scanning system anymore, but rather measure only linearly. In a second step, the LiDAR-derived snow depth, SWE and grain size maps then will be validated using an extensive measurement setup installed at the Schauinsland and in the Alptal, Switzerland. At both plots, a network of 39 standalone snow monitoring stations (SnoMoS)[1,76] in total are placed in characteristic locations for monitoring a variety of different forest processes and canopy properties. These measurements will be further complemented by repeated manual snow surveys aimed at deriving snow density, liquid water content and grain sizes along representative transects. The resulting unique data set will allow the application of recent snow models like SNOWPACK/ALPINE 3D[67] and FSM2[68] to the study sites, co-registration of the LiDAR-derived point clouds and validation of the derived products.

Additionally, similar to the novel LiDAR scanner the VLP-16 on the Delta Quad will also be equipped with an APX-15 integrated INS solution to improve the accuracy of the geo-referenced point cloud for quantitative analysis; this setup also allows for additional cross-validation of large-scale snow depth maps by an independent LiDAR scanning platform. Further validation data on smaller scales will be gathered by a third system, the lightweight airborne profiler (LAP) developed at Fraunhofer Institute for Physical Measurement Techniques IPM. This sensor also operates as a time-of-flight LiDAR scanner, but with a wavelength of 905 nm and is equipped with two RGB-cameras for later point cloud colorization.[77] Furthermore, simulations of the BRDF will be needed for correcting the LiDAR data for view angle related intensity variations, e.g. at steep slopes. Alternatively, these issues might be addressed by appropriate flight planning also accounting for other flight trajectory related error sources as described in.[6]

## 5. CONCLUSION

In this work, we first summarized the current state of the art of airborne LiDAR remote sensing of snow depth and SWE. So far, there exists no system that combines both, snow depth mapping and information of the water content of the snowpack in a single LiDAR sensor. More specifically, the entire field of LiDAR snow depth mapping with UAV platforms in general is still in its infancy, so further research is urgently needed. Based on the spectral dependence of snow reflectance on snow grain size, grain shape, snow density, liquid water content and shallow snow depths summarized subsequently, we outlined a detailed concept of a lightweight dual-wavelength LiDAR sensor that can be mounted to common UAVs like multicopters. Operating at two wavelengths $\lambda_1 = 1030\,\mathrm{nm}$ and $\lambda_2 = 515\,\mathrm{nm}$, the sensor does not only map the topography of a snowpack, but also collects spectral information for each data point. Comparing the back-reflected intensities for the two wavelengths, information about the snowpack like the effective grain size can be deduced. By feeding these information back into state-of-the-art snow models, coherent snow density and – using the topography maps – SWE will be computed. Finally, we complemented our system proposal by conceptual LiDAR measurements on snow using a commercially existing Velodyne Puck VLP-16 LiDAR scanner. We tested its capability to measure snow depth, pointing out that the VLP-16 tends to underestimate the snow depth systematically, but still within the stated accuracy of $\pm 3\,\mathrm{cm}$. By mounting the sensor to a VTOL UAV, we collected airborne LiDAR data on snow at a mid elevation mountainside in the Black Forest, demonstrating its capability to monitor a snowpack in open fields as well in forested areas. Finally, we investigated the view angle-dependent back-scattered intensity of snow, showing that due to the strongly forward-scattering characteristics of snow, intensity decreases more strongly at larger view angles than for a grass lawn. As a consequence, in case of our novel LiDAR sensor in the future special attention has to be dedicated to the quantitative analysis of back-scattered intensities since there are several factors impacting these. Prospectively, remotely sensed snow depth and SWE maps will be validated against ground data collected by a permanently installed network of snow monitoring stations, as well as manual field measurements.

## ACKNOWLEDGMENTS

This work is part of the project "Understanding and Predicting the Spatial and Temporal Variability of Snow Processes Under Different Vegetation Covers Combining Laser Observations and Point Measurements SPENSER" funded by the Deutsche Forschungsgemeinschaft (DFG, German Research Foundation) - project number 443637229.

## REFERENCES

[1] Pohl, S., Garvelmann, J., Wawerla, J., and Weiler, M., "Potential of a low-cost sensor network to understand the spatial and temporal dynamics of a mountain snow cover," *Water Resources Research* **50**(3), 2533–2550 (2014).

[2] Ryan, W. A., Doesken, N. J., and Fassnacht, S. R., "Evaluation of Ultrasonic Snow Depth Sensors for U.S. Snow Measurements," *Journal of Atmospheric and Oceanic Technology* **25**(5), 667–684 (2008).

[3] Pirazzini, R., Leppänen, L., Picard, G., Lopez-Moreno, J. I., Marty, C., Macelloni, G., Kontu, A., von Lerber, A., Tanis, C. M., Schneebeli, M., de Rosnay, P., and Arslan, A. N., "European In-Situ Snow Measurements: Practices and Purposes," *Sensors (Basel, Switzerland)* **18**(7) (2018).

[4] Lievens, H., Demuzere, M., Marshall, H.-P., Reichle, R. H., Brucker, L., Brangers, I., de Rosnay, P., Dumont, M., Girotto, M., Immerzeel, W. W., Jonas, T., Kim, E. J., Koch, I., Marty, C., Saloranta, T., Schöber, J., and de Lannoy, G. J. M., "Snow depth variability in the Northern Hemisphere mountains observed from space," *Nature communications* **10**(1), 4629 (2019).

[5] Nolin, A. W., "Recent advances in remote sensing of seasonal snow," *Journal of Glaciology* **56**(200), 1141–1150 (2010).

[6] Deems, J. S., Painter, T. H., and Finnegan, D. C., "Lidar measurement of snow depth: a review," *Journal of Glaciology* **59**(215), 467–479 (2013).

[7] Painter, T. H., Berisford, D. F., Boardman, J. W., Bormann, K. J., Deems, J. S., Gehrke, F., Hedrick, A., Joyce, M., Laidlaw, R., Marks, D., Mattmann, C., McGurk, B., Ramirez, P., Richardson, M., Skiles, S. M., Seidel, F. C., and Winstral, A., "The Airborne Snow Observatory: Fusion of scanning lidar, imaging spectrometer, and physically-based modeling for mapping snow water equivalent and snow albedo," *Remote Sensing of Environment* **184**, 139–152 (2016).

[8] Harder, P., Pomeroy, J. W., and Helgason, W. D., "Improving sub-canopy snow depth mapping with unmanned aerial vehicles: lidar versus structure-from-motion techniques," *The Cryosphere* **14**(6), 1919–1935 (2020).

[9] Knoebl, K., Schattan, P., Fey, C., and Wichmann, V., "Analysis of the Spatio-Temporal Development of Snow Surface Wetness in a High Alpine Area Using Terrestrial Laser Scanning Reflectivity," *Proceedings of the International Snow Science Workshop* (2018).

[10] Fey, C., Schattan, P., Helfricht, K., and Schöber, J., "A compilation of multitemporal TLS snow depth distribution maps at the Weisssee snow research site (Kaunertal, Austria)," *Water Resources Research* (2019).

[11] Broxton, P. D. and van Leeuwen, W. J. D., "Structure from Motion of Multi-Angle RPAS Imagery Complements Larger-Scale Airborne Lidar Data for Cost-Effective Snow Monitoring in Mountain Forests," *Remote Sensing* **12**(14), 2311 (2020).

[12] Jacobs, J. M., Hunsaker, A. G., Sullivan, F. B., Palace, M., Burakowski, E. A., Herrick, C., and Cho, E., "Snow depth mapping with unpiloted aerial system lidar observations: a case study in Durham, New Hampshire, United States," *The Cryosphere* **15**(3), 1485–1500 (2021).

[13] Sturm, M., Taras, B., Liston, G. E., Derksen, C., Jonas, T., and Lea, J., "Estimating Snow Water Equivalent Using Snow Depth Data and Climate Classes," *Journal of Hydrometeorology* **11**(6), 1380–1394 (2010).

[14] Broxton, P. D., Leeuwen, W. J. D., and Biederman, J. A., "Improving Snow Water Equivalent Maps With Machine Learning of Snow Survey and Lidar Measurements," *Water Resources Research* **55**(5), 3739–3757 (2019).

[15] Smyth, E. J., Raleigh, M. S., and Small, E. E., "Particle Filter Data Assimilation of Monthly Snow Depth Observations Improves Estimation of Snow Density and SWE," *Water Resources Research* **55**(2), 1296–1311 (2019).

[16] Winkler, M., Schellander, H., and Gruber, S., "Snow water equivalents exclusively from snow depths and their temporal changes: the Dsnow model," *Hydrology and Earth System Sciences* **25**(3), 1165–1187 (2021).

[17] Chang, A. T. C., Foster, J. L., and Hall, D. K., "Effects of Forest on the Snow Parameters Derived from Microwave Measurements During the Boreas Winter Field Campaign," *Hydrological Processes* **10**(12), 1565–1574 (1996).

[18] Luojus, K., Pullianinen, J., Takala, M., Lemmetyinen, J., Kangwa, M., Smolander, T., Derksen, C., and Pinnock, S., "ESA Globsnow: Algorithm Theoretical Basis Document-SWE-algorithm," (2013).

[19] Goodison, B. E. and Walker, A. E.., "Canadian development and use of snow cover information from passive microwave satellite data," in [*Passive Microwave Remote Sensing of Land-Atmosphere Interactions*], 245–262, De Gruyter (1995).

[20] Carroll, T., "Airborne gamma radiation snow survey program: a user's guide, version 5.0," *National Operational Hydrologic Remote Sensing Center (NOHRSC), Chanhassen* **14** (2001).

[21] Guneriussen, T., Hogda, K. A., Johnsen, H., and Lauknes, I., "InSAR for estimation of changes in snow water equivalent of dry snow," *IEEE Transactions on Geoscience and Remote Sensing* **39**(10), 2101–2108 (2001).

[22] Rott, H., Nagler, T., & Scheiber, R., "Snow mass retrieval by means of SAR interferometry," *3rd FRINGE Workshop, European Space Agency, Earth Observation* **III** (2003).

[23] Leinss, S., Wiesmann, A., Lemmetyinen, J., and Hajnsek, I., "Snow Water Equivalent of Dry Snow Measured by Differential Interferometry," *IEEE Journal of Selected Topics in Applied Earth Observations and Remote Sensing* **8**(8), 3773–3790 (2015).

[24] Webb, R. W., Jennings, K. S., Fend, M., and Molotch, N. P., "Combining Ground–Penetrating Radar With Terrestrial LiDAR Scanning to Estimate the Spatial Distribution of Liquid Water Content in Seasonal Snowpacks," *Water Resources Research* **54**(12) (2018).

[25] Pomerleau, P., Royer, A., Langlois, A., Cliche, P., Courtemanche, B., Madore, J.-B., Picard, G., and Lefebvre, É., "Low Cost and Compact FMCW 24 GHz Radar Applications for Snowpack and Ice Thickness Measurements," *Sensors (Basel, Switzerland)* **20**(14) (2020).

[26] Bair, E. H., Abreu Calfa, A., Rittger, K., and Dozier, J., "Using machine learning for real-time estimates of snow water equivalent in the watersheds of Afghanistan," *The Cryosphere* **12**(5), 1579–1594 (2018).

[27] Judson, A. and Doesken, N., "Density of Freshly Fallen Snow in the Central Rocky Mountains," *Bulletin of the American Meteorological Society* **81**(7), 1577–1587 (2000).

[28] Roebber, P. J., Bruening, S. L., Schultz, D. M., and Cortinas, J. V., "Improving Snowfall Forecasting by Diagnosing Snow Density," *Weather and Forecasting* **18**(2), 264–287 (2003).

[29] Spencer, M. K., Alley, R. B., and Creyts, T. T., "Preliminary firn-densification model with 38-site dataset," *Journal of Glaciology* **47**(159), 671–676 (2001).

[30] Anderson, D. L. and Benson, C. S., "The densification and diagenesis of snow," (1963).

[31] Marks, D., Domingo, J., Susong, D., Link, T., and Garen, D., "A spatially distributed energy balance snowmelt model for application in mountain basins," *Hydrological Processes* **13**(12-13), 1935–1959 (1999).

[32] He, C. and Flanner, M., "Snow Albedo and Radiative Transfer: Theory, Modeling, and Parameterization," in [*Springer Series in Light Scattering*], Kokhanovsky, A., ed., 67–133, Springer International Publishing, Cham (2020).

[33] Segelstein, D. J., "The Complex Refractive Index of Water."

[34] Warren, S. G. and Brandt, R. E., "Optical constants of ice from the ultraviolet to the microwave: A revised compilation," *Journal of Geophysical Research* **113**(D14) (2008).

[35] Schaepman-Strub, G., Schaepman, M. E., Painter, T. H., Dangel, S., and Martonchik, J. V., "Reflectance quantities in optical remote sensing—definitions and case studies," *Remote Sensing of Environment* **103**(1), 27–42 (2006).

[36] Nicodemus, F. E., Richmond, J. C., Hsia, J. J., Ginsberg, I. W., and Limperis, T., "Geometrical considerations and nomenclature for reflectance," in [*Radiometry*], 94–145, Jones and Bartlett Publishers, Inc (1992).

[37] Warren, S. G., "Optical properties of snow," *Reviews of Geophysics* **20**(1), 67 (1982).

[38] Wiscombe, W. J. and Warren, S. G., "A Model for the Spectral Albedo of Snow. I: Pure Snow," *Journal of the Atmospheric Sciences* **37**(12), 2712–2733 (1980).

[39] Mie, G., "Beiträge zur Optik trüber Medien, speziell kolloidaler Metallösungen," *Annalen der Physik* **330**(3), 377–445 (1908).

[40] van de Hulst, H. C., [*Light Scattering by Small Particles*], Dover Publications (1981).

[41] Nolin, A. W. and Dozier, J., "Estimating snow grain size using AVIRIS data," *Remote Sensing of Environment* **44**(2-3), 231–238 (1993).

[42] Nolin, A. W. and Dozier, J., "A Hyperspectral Method for Remotely Sensing the Grain Size of Snow," *Remote Sensing of Environment* **74**(2), 207–216 (2000).

[43] Dozier, J. and Painter, T. H., "Multispectral and Hyperspectral Remote Ssensing of Alpine Snow Properties," *Annual Review of Earth and Planetary Sciences* **32**(1), 465–494 (2004).

[44] Dozier, J., Schneider, S. R., and McGinnis, D. F., "Effect of grain size and snowpack water equivalence on visible and near-infrared satellite observations of snow," *Water Resources Research* **17**(4), 1213–1221 (1981).

[45] Green, R. O., Dozier, J., Roberts, D., and Painter, T., "Spectral snow-reflectance models for grain-size and liquid-water fraction in melting snow for the solar-reflected spectrum," *Annals of Glaciology* **34**, 71–73 (2002).

[46] O'Brien, H. W. and Munis, R. H., "Red and Near-infrared Spectral Reflectance of Snow."

[47] Dozier, J., Davis, R., Chang, A., and Brown, K., "The spectral bidirectional reflectance of snow," (1988).

[48] Bohren, C. F. and Beschta, R. L., "Snowpack albedo and snow density," *Cold Regions Science and Technology* **1**(1), 47–50 (1979).

[49] Deems, J. S., Gadomski, P. J., Vellone, D., Evanczyk, R., LeWinter, A. L., Birkeland, K. W., and Finnegan, D. C., "Mapping starting zone snow depth with a ground-based lidar to assist avalanche control and forecasting," *Cold Regions Science and Technology* **120**, 197–204 (2015).

[50] Perovich, D. K., "Light reflection and transmission by a temperate snow cover," *Journal of Glaciology* **53**(181), 201–210 (2007).

[51] Nolin, A. W., Steffen, K., and Dozier, J., "Measurement and modeling of the bidirectional reflectance of snow," in [*Proceedings of IGARSS '94 - 1994 IEEE International Geoscience and Remote Sensing Symposium*], 1919–1921, IEEE (1994).

[52] Painter, T. H. and Dozier, J., "The effect of anisotropic reflectance on imaging spectroscopy of snow properties," *Remote Sensing of Environment* **89**(4), 409–422 (2004).

[53] Stamnes, K., Tsay, S. C., Wiscombe, W., and Jayaweera, K., "Numerically stable algorithm for discrete-ordinate-method radiative transfer in multiple scattering and emitting layered media," *Applied optics* **27**(12), 2502–2509 (1988).

[54] Painter, T. H., "Measurements of the hemispherical-directional reflectance of snow at fine spectral and angular resolution," *Journal of Geophysical Research* **109**(D18) (2004).

[55] Libbrecht, K. G., "The physics of snow crystals," *Reports on Progress in Physics* **68**(4), 855–895 (2005).

[56] Nichols, H. B., "Snow Crystals: Natural and Artificial. Ukichiro Nakaya. Harvard Univ. Press, Cambridge, 1954. xii + 510 pp.," *Science* **120**(3123), 755 (1954).

[57] Leroux, C., Deuzé, J.-L., Goloub, P., Sergent, C., and Fily, M., "Ground measurements of the polarized bidirectional reflectance of snow in the near-infrared spectral domain: Comparisons with model results," *Journal of Geophysical Research: Atmospheres* **103**(D16), 19721–19731 (1998).

[58] Leroux, C., Lenoble, J., Brogniez, G., Hovenier, J. W., and de Haan, J. F., "A Model for the Bidirectional Polarized Reflectance of Snow," *Journal of Quantitative Spectroscopy and Radiative Transfer* **61**(3), 273–285 (1999).

[59] Kokhanovsky, A. A. and Zege, E. P., "Scattering optics of snow," *Applied optics* **43**(7), 1589–1602 (2004).

[60] Grenfell, T. C., Perovich, D. K., and Ogren, J. A., "Spectral albedos of an alpine snowpack," *Cold Regions Science and Technology* **4**(2), 121–127 (1981).

[61] Aoki, T., Aoki, T., Fukabori, M., Hachikubo, A., Tachibana, Y., and Nishio, F., "Effects of snow physical parameters on spectral albedo and bidirectional reflectance of snow surface," *Journal of Geophysical Research: Atmospheres* **105**(D8), 10219–10236 (2000).

[62] He, C., Takano, Y., Liou, K.-N., Yang, P., Li, Q., and Chen, F., "Impact of Snow Grain Shape and Black Carbon–Snow Internal Mixing on Snow Optical Properties: Parameterizations for Climate Models," *Journal of Climate* **30**(24), 10019–10036 (2017).

[63] Warren, S. G. and Wiscombe, W. J., "A Model for the Spectral Albedo of Snow. II: Snow Containing Atmospheric Aerosols," *Journal of the Atmospheric Sciences* **37**(12), 2734–2745 (1980).

[64] He, C., Liou, K.-N., and Takano, Y., "Resolving Size Distribution of Black Carbon Internally Mixed With Snow: Impact on Snow Optical Properties and Albedo," *Geophysical Research Letters* **45**(6), 2697–2705 (2018).

[65] He, C., Flanner, M. G., Chen, F., Barlage, M., Liou, K.-N., Kang, S., Ming, J., and Qian, Y., "Black carbon-induced snow albedo reduction over the Tibetan Plateau: uncertainties from snow grain shape and aerosol–snow mixing state based on an updated SNICAR model," *Atmospheric Chemistry and Physics* **18**(15), 11507–11527 (2018).

[66] Rieger, P., "Range ambiguity resolution technique applying pulse-position modulation in time-of-flight scanning lidar applications," *Optical Engineering* **53**(6), 061614 (2014).

[67] Gouttevin, I., Lehning, M., Jonas, T., Gustafsson, D., and Mölder, M., "A two-layer canopy model with thermal inertia for an improved snowpack energy balance below needleleaf forest (model SNOWPACK, version 3.2.1, revision 741)," *Geoscientific Model Development* **8**(8), 2379–2398 (2015).

[68] Mazzotti, G., Essery, R., Moeser, C. D., and Jonas, T., "Resolving Small–Scale Forest Snow Patterns Using an Energy Balance Snow Model With a One–Layer Canopy," *Water Resources Research* **56**(1) (2020).

[69] Mallet, C. and Bretar, F., "Full-waveform topographic lidar: State-of-the-art," *ISPRS Journal of Photogrammetry and Remote Sensing* **64**(1), 1–16 (2009).

[70] Lefsky, M. A., Cohen, W. B., Parker, G. G., and Harding, D. J., "Lidar Remote Sensing for Ecosystem Studies," *BioScience* **52**(1), 19 (2002).

[71] Yunfei, B., Guoping, L., Chunxiang, C., Xiaowen, L., Hao, Z., Qisheng, H., Linyan, B., and Chaoyi, C., "Classification of LIDAR point cloud and generation of DTM from LIDAR height and intensity data in forested area," *The International Archives of the Photogrammetry, Remote Sensing and Spatial Information Sciences* **37**(7), 313–318 (2008).

[72] Velodyne LiDAR, Inc., "VLP-16 User Manual," (2019).

[73] Glennie, C., Kusari, A., and Facchin, A., "Calibration and Stability Analysis of the VLP-16 Laser Scanner," *ISPRS - International Archives of the Photogrammetry, Remote Sensing and Spatial Information Sciences* **XL-3/W4**, 55–60 (2016).

[74] Bula, J., Derron, M.-H., and Mariethoz, G., "Dense point cloud acquisition with a low-cost Velodyne VLP-16," *Geoscientific Instrumentation, Methods and Data Systems* **9**(2), 385–396 (2020).

[75] Warren, S. G., "Can black carbon in snow be detected by remote sensing?," *Journal of Geophysical Research: Atmospheres* **118**(2), 779–786 (2013).

[76] Varhola, A., Wawerla, J., Weiler, M., Coops, N. C., Bewley, D., and Alila, Y., "A New Low-Cost, Stand-Alone Sensor System for Snow Monitoring," *Journal of Atmospheric and Oceanic Technology* **27**(12), 1973–1978 (2010).

[77] Becker, D., Stemmler, S., and Reiterer, A., "Entwicklung und Evaluierung eines kompakten Multisensorsystems für den Einsatz auf Drohnen," in [*Ingenieurvermessung 20*], **X**, 99–108, Wichmann.